AIAA JOURNAL
Vol. 44, No. 12, December 2006

Separation Control Using Plasma Actuators: Dynamic Stall Vortex Control on Oscillating Airfoil

Martiqua L. Post*
U. S. Air Force Academy, Colorado Springs, Colorado 80840
and
Thomas C. Corke†
University of Notre Dame, Notre Dame, Indiana 46556

DOI: 10.2514/1.22716

A plasma actuator was used to control leading-edge flow separation and dynamic stall vortex on a periodically oscillated NACA 0015 airfoil. The effectiveness of the actuator was documented through phase-conditioned surface pressure measurements and smoke flow visualization records. The airfoil was driven in a periodic cycle corresponding to $\alpha = 15\,\text{deg} + 10\,\text{deg}\,\sin\omega t$. The results presented here are for a reduced frequency of $k = \omega c/2U_\infty = 0.08$. Three cases of control with the plasma actuator were investigated: open-loop control with steady plasma actuation, open-loop control with unsteady plasma actuation, and closed-loop control with steady plasma actuation. For closed-loop control, the actuator was activated in selected portions of the oscillatory cycle based on angle-of-attack feedback. All of the cases investigated exhibited an increase in cycle-integrated lift with improvements in the lift-cycle hysteresis. In two cases, the pitch-moment stall angle was delayed and in one of these, the adverse negative moment peak was significantly reduced.

Nomenclature

C_d	=	coefficient of drag
C_l	=	coefficient of lift
C_m	=	moment coefficient
C_p	=	coefficient of pressure
c	=	chord
$\boldsymbol{E}$	=	electric field strength vector
$\boldsymbol{F}_B$	=	body force vector
k	=	reduced frequency
Re_c	=	chord Reynolds number
U	=	local velocity
V	=	voltage
x	=	distance in the x direction
α	=	angle of attack
ϵ_o	=	permittivity of free space
λ_D	=	Debye length
ϕ	=	local electric potential
ω	=	physical pitch oscillating frequency

I. Introduction

HIGH-performance future rotorcraft will require significant improvements in multiple attributes including increased range for global self-deployabilty, increased performance for fast agile missions, increased payload, and reduced external noise emissions, cabin noise, and vibration. Retreating blade stall ultimately establishes the limits on rotor load and flight speed. In addition to the loss of capability to generate lift, unsteady blade stall transmits large impulsive blade pitching moments to the flight control system [1]. To prevent excessive control loads, a stall boundary must be set to define the maximum blade load capability as a function of rotor load and flight speed. These limits impact maneuverability and agility as well as speed and payload. Aiken et al. [2] point out that if the stall angle of attack can be extended beyond the range of helicopter blade pitch control inputs, a revolutionary new concept will become a reality: the stall-free rotor. The implications for rotorcraft will be of great significance by removing retreating blade stall as a major flying-qualities constraint [2].

The flow physics involved in blade stall is leading-edge boundary-layer separation that occurs during rapid motion to high blade angle of attack. The dynamic stall phenomenon has been extensively studied using pitching airfoil and three-dimensional blade sections on both model and full scales [3–5] and by numerical simulations [6–8]. At full scale, reduced frequencies are typically $0.05 \leq k \leq 0.15$ with maximum instantaneous pitch rates of $0.002 \leq A \leq 0.02$. The relative external flow Mach numbers range from 0.3 to 0.5, whereas the peak local Mach numbers near the separation location of $0.05 \leq x/C \leq 0.15$ are typically from 1.1 to 1.3. The full-scale Reynolds numbers are about $Re_c = 4 \times 10^6$.

Stalled flow locations on the rotor disk have been identified by surface pressure measurements during flight tests of full-scale aircraft [9] and by surface pressure, heat transfer, and tuft measurements in wind-tunnel tests of model rotors [10]. The combination of detailed unsteady airfoil experiments, computations, and global rotor measurements on maneuvering aircraft [11] has defined the retreating blade stall phenomena that must be controlled and the conditions under which the control is required.

The passive devices typically effective on fixed wings [12] are impractical on helicopter rotors because they would have to be deployed in a rapid, time-dependent manner in the rotor cycle. For example, although recent studies [13] have explored the application of leading-edge slots to delay stall on helicopter rotors, they incur a high drag penalty at low angles of attack of the advancing blade in high-speed forward flight. In addition, the helicopter rotor is a finely engineered composite structure that has to be able to withstand high centrifugal loading. Any moving or deployable elements on the rotor would be subjected to the same high loading levels. Even the addition of slots or internal cavities in the rotor that are needed for steady or unsteady surface blowing could present a significant compromise in the structural integrity of the rotor.

Steady flow control methods such as air injection [14] or suction [15] have been investigated, but transferring sufficient fluid from the fixed to the rotating frame at acceptable levels of power and complexity presents significant difficulties. Successful application of

Received 25 January 2006; revision received 7 July 2006; accepted for publication 11 July 2006.

*Assistant Professor, Department of Aeronautics. Senior Member AIAA.
†Clark Chair Professor, Center for Flow Physics and Control, Aerospace and Mechanical Engineering Department. Associate Fellow AIAA.

flow control to the rotor blade will require the development of new and innovative technologies that integrate a thorough understanding of the underlying fluid dynamics with a robust and efficient actuation, sensing, and control system.

Our approach to separation control on both fixed wings and helicopter rotors is the use of single dielectric barrier discharge (SDBD) plasma actuators [16]. These have a number of distinct advantages over other active flow control devices:

1) They are fully electronic with no mechanical parts and, therefore, are able to withstand high force loading.

2) They can be laminated onto wing surfaces and, therefore, they do not require slots or cavities.

3) They have a broad frequency-response bandwidth so that they can have fast response for feedback control.

The plasma actuator consists of two copper electrodes separated by a dielectric insulator. The electrodes are supplied with a high-order (3–12 kV_{p-p}) ac voltage. When the voltage is sufficiently high, the surrounding air ionizes and plasma forms in the regions of high electrical field potential. These regions are generally located at the edges of the electrode(s) exposed to the air. The ionized air, in the presence of an electric field gradient, results in a body force on the flow [17]. The body force is a vector that can be tailored for a given application through the orientation and design of the electrode geometry.

The actuators can be operated either in a quasi-steady or unsteady manner. In the quasi-steady manner, the operating ac frequency is well above the fluid response frequency and, therefore, senses a constant body force.

In the unsteady manner, the operating ac frequency is impulsively switched on and off at a lower frequency. It has been shown in the literature that the introduction of unsteady disturbances near the separation location can cause the generation of large coherent vortical structures that could prevent or delay the onset of separation. These structures are thought to intermittently bring high momentum fluid to the surface, enabling the flow to withstand the adverse pressure gradient without separating. Periodic excitation by oscillatory blowing for use in separation control has been documented extensively by Seifert, et al. [18–20] and in the review by Greenblatt and Wygnanski [21]. Operating the plasma in the unsteady manner with a short duty cycle reduces the actuator power significantly.

The SDBD plasma actuators have been successfully used in numerous flow control applications. These include lift augmentation on a wing section [22], low-pressure turbine blade separation control [23], airfoil leading-edge separation control [16,24], and plasma flaps and slats [25]. Wilkinson [26] attempted to simulate the effects of an oscillating wall by means of phased plasma arrays. Thomas et al. [27] demonstrated bluff body separation control for the purpose of landing gear noise reduction. Hultgren and Ashpis [28] used an array of plasma actuators to affect separation in a wind-tunnel section that was designed to produce the same streamwise pressure gradient as on the suction surface of a PakB blade.

The object of our research was to use the SDBD plasma actuator to control the dynamic stall vortex on oscillating airfoils. The application of this is toward controlling retreating blade stall on helicopter rotors. Our objective was to model as much of the essential physics as possible in the experiments. For this, a representative reduced frequency was used. The flow control approach focused on the use of the SDBD plasma actuators.

II. Experimental Setup

The experiments were conducted in one of the subsonic wind tunnels in the Center for Flow Physics and Control (FlowPAC) in the Hessert Laboratory at the University of Notre Dame. The facility is an open-return wind tunnel with a 0.61 by 0.61 m (2 $ftft^2$) by 1.8 m (6 ft) long test section. The tunnel consists of a removable inlet having a series of 12 screens followed by an 18:1 contraction that attaches to the test section. The test section is equipped with a Plexiglas wall and a glass floor that allow optical access when flow visualization is performed. The back wall of the test section was used to mount the airfoil. Removable hatch doors in the back wall provided access into the test section. A schematic of the wind tunnel is shown in Fig. 1.

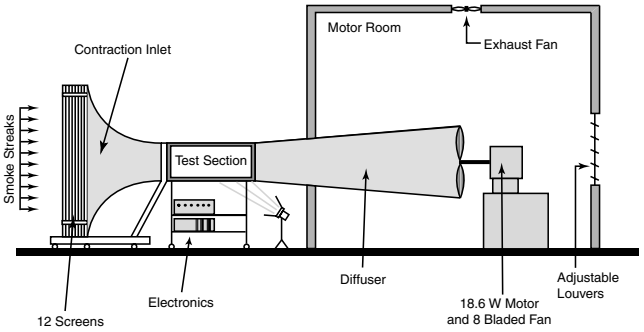

Fig. 1 Schematic of open-return wind tunnel used in the experiments.

A. Airfoil

The airfoil used in this study was a NACA 0015. This shape was chosen because it exhibits well-known and documented steady characteristics as well as leading-edge separation at large angles of attack. Also, the NACA 0015 airfoil has commonly been used for helicopter rotor blades and numerous experimental results for its oscillating conditions exist in the literature.

The airfoil had a 12.7 cm (5 in.) chord and a 25.4 cm (10 in.) span. The size of the airfoil was chosen to minimize blockage effects, especially at the large angles of attack that were investigated. At an angle of attack of 25 deg, the blockage was only 4%. Details of the airfoil's manufacturing process can be found in Post and Corke [24].

End plates were used to minimize 3-D end effects on the airfoil. The end plates were constructed from clear Plexiglas to allow visual access for flow visualization over the surface of the airfoil. The end plates were round, with a 40 cm (15.75 in.) diameter. The center of the circular end plates was at the airfoil's pitch location, which corresponded to the quarter-chord location. With this configuration, the end plates appeared stationary in the flow visualization results. Figure 2 shows a schematic drawing of the airfoil and a photograph outside the tunnel test section.

The airfoil was capable of being oscillated or dynamically pitched about its quarter-chord location with any mean and alternating angles. The pitching motion was driven by a specially selected servo motor (SmartMotor SM3430 by Animatics). This had a 10:1 gear drive and provided 11 N · m (96.8 psi) of continuous torque. The motor controller was built into the motor, and the SmartMotor

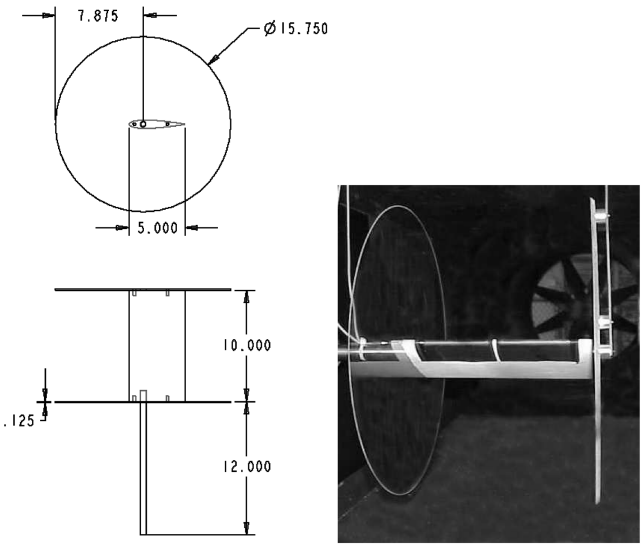

Fig. 2 Schematic drawing (top) and photograph (bottom) of 12.7 cm (5 in.) chord airfoil with end plates. Dimensions are in inches.

Table 1 Pressure port locations

Port no.	x/c	Port no.	x/c
0	0.0		
1/2	0.025	15/16	0.456
3/4	0.051	17/18	0.532
5/6	0.076	19/20	0.608
7/8	0.152	21/22	0.684
9/10	0.228	23/24	0.759
11/12	0.304	25/26	0.835
13/14	0.380	27/28	0.911

Interface software was used to modify the controller program. Two encoder signals were used to determine the instantaneous position of the motor.

B. Pressure Data Acquisition

A total of 29 surface pressure ports, 0.5 mm (0.02 in.) i.d., were aligned with the flow direction at the half-span location on the airfoil. Although they were spaced relatively uniformly around the airfoil, there was a slight increase in concentration of ports near the leading edge. Table 1 provides the positions of the surface pressure ports.

The pressure measurements were made using a Scanivalve Model J9 scanning pressure valve with a single Scanivalve PDCR24 differential pressure transducer having a range of ± 10 in H_2O. All of the pressure tubing was kept as short as possible to maximize the dynamic response. The total pressure measurement system was dynamically calibrated and was found to have a flat response within 3 dB, up to 150 Hz. A pitot static probe in the freestream provided the reference static pressure for each pressure port.

Data acquisition was performed using a customized LabView program. The pressure acquisition system worked as follows: 1) a pressure port was selected, 2) a time delay occurred to allow for the response of the Scanivalve, 3) pressure–time series were acquired in a continuous record for a user-defined number of pitching cycles, (4) the time-series record was stored, (5) a cycle-based ensemble average and standard deviations were computed and stored, and (6) another pressure port was selected and the acquisition steps were repeated until all of the pressure ports had been sampled.

C. Flow Visualization

Flow visualization was done by introducing continuous smoke streaklines upstream of the wind-tunnel screens and contraction. A description of the smoke generator is given by Mueller [29]. The smoke emanated from a rake of tubes as low-speed laminar jets. The tubes were aligned in the vertical direction and located at the spanwise centerline. The smoke streaks were drawn into the tunnel inlet and converged into a closely spaced, vertically aligned group following the contraction.

The airfoil was illuminated using a strobe light source. The light passed through a glass slot in the floor of the test section. It was externally triggered by the motor encoder output at specific angles of attack to obtain phase-conditioned visualization records. The flow visualization records were made using a Panasonic analog video camera. The videotape was digitized through a video capture card where individual frames were extracted.

D. Plasma Actuator

The plasma actuator consisted of two copper electrodes separated by a dielectric insulator, as illustrated in the schematic in Fig. 3. The copper electrodes were made from 0.0254-mm thick copper foil tape. The width of the exposed electrode was 12.7 mm and the insulated electrode was 50.8 mm. The dielectric insulator was 5-mil (0.127 mm) thick Kapton film tape. As illustrated in Fig. 3, the electrodes were arranged in an asymmetric arrangement with an overlap of 1 mm.

The plasma actuator was bonded directly to the surface of the airfoil. The NACA 0015 airfoil was cast with a recess for the actuator at the leading edge, so that when the plasma actuator was applied it

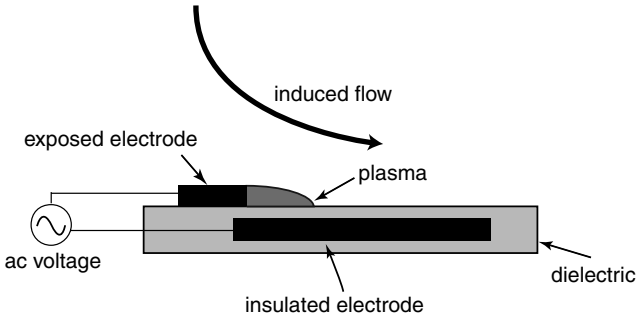

Fig. 3 Schematic of asymmetric plasma actuators arrangement used in these experiments.

produced a smooth, flush surface with the NACA 0015 airfoil shape. Both the exposed and insulated electrodes spanned the airfoil; however, a necessary, narrow gap was left at the location of the pressure ports. This narrow gap was approximately 6 mm and is visible in the photograph in Fig. 2.

The plasma actuator was located at the leading edge ($x/c = 0$). This means that the overlapping edge of the exposed electrode was at $x/c = 0$. In this arrangement, the plasma actuator was oriented to produce a velocity component in the mean freestream direction over the suction surface of the airfoil. Based on particle image velocimetry (PIV) measurements in quiescent air for the actuator voltages used, the maximum of this velocity component is expected to be of the order of 2–3 m/s [16] measured approximately 2 cm downstream of the edge of the exposed electrode. It is considered to be uniform in the spanwise direction, although no direct measurements were made in this experiment.

The signal supplied to the plasma actuator was a 5 kHz triangle wave with an ac voltage of 11 kV_{p-p}. The circuit used to generate the plasma is shown in Fig. 4. For the steady operation, the 5 kHz triangle wave signal was constantly supplied to both the exposed and insulated electrodes. The power used by the steady actuator was 20 W · ft span. For the unsteady operation, the same 5 kHz triangle wave was used to generate the plasma, but it was cycled off and on with an unsteady period T, as illustrated in Fig. 5. The percentage of

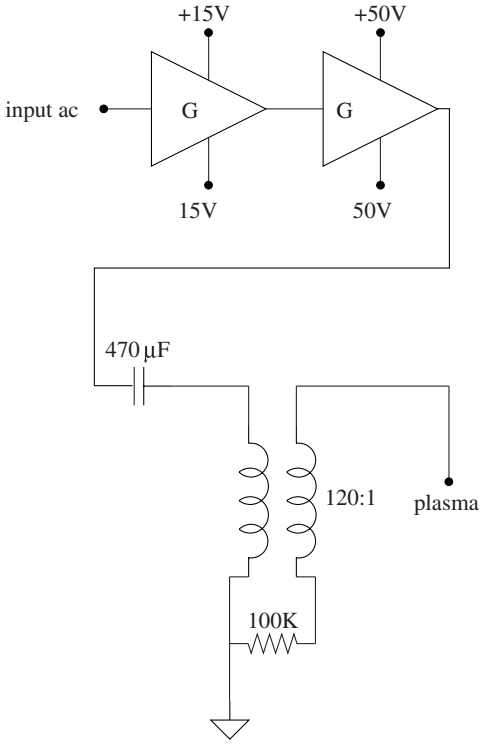

Fig. 4 Schematic of circuit used to generate the plasma.

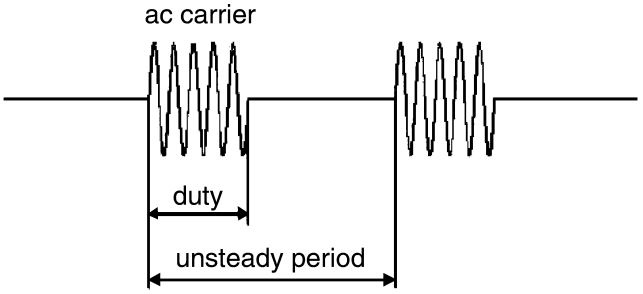

Fig. 5 Illustration of plasma actuator time series used for unsteady actuation.

time within the period that the ac voltage was on, called the duty cycle, was controllable. It was found that for unsteady actuator operation, a duty cycle of only 10% was sufficient to achieve flow control. Because the unsteady actuator was only operating for one-tenth of the time of the steady actuator, the power to the actuator was 90% less, giving a nominal value of 2 W per foot span.

In the asymmetric electrode arrangement shown in Fig. 3, plasma forms in the air at the edge of the exposed electrode and extends on the dielectric over the lower insulated electrode. The asymmetric arrangement produces an electric field gradient that in the presence of the plasma, results in a body force vector per unit volume of plasma [17,30] given as

$$\frac{\boldsymbol{F}_B}{V} = \left(\frac{\epsilon_o}{\lambda_D^2}\phi\right)\boldsymbol{E} \tag{1}$$

The electric potential and electric field vector [17] are related through the following equation:

$$\boldsymbol{E} = \boldsymbol{\Delta}\phi \tag{2}$$

The unsteady body force vector and flow response for an asymmetric electrode arrangement like that used here results in an induced flow in the direction of the lower electrode (from left to right in Fig. 3).

III. Results

The results presented here demonstrate the effectiveness of the plasma actuator to control the dynamic stall vortex. The NACA 0015 airfoil was oscillated in a periodic cycle about its quarter-chord location as

$$\alpha = \alpha_{\text{mean}} + \alpha_{\text{max}} \sin \omega t$$

The full experiment examined a large range of parameters including different α_{mean}, α_{max}, and normalized frequencies $k = \omega c/2U_\infty$. These results correspond to one condition, based on the operating conditions of helicopter rotors, with $\alpha_{\text{mean}} = 15$ deg, $\alpha_{\text{max}} = 10$ deg, and $k = 0.08$. For this reduced frequency, the physical pitch oscillating frequency was 4 Hz. The freestream speed used for all quantitative (surface pressure measurements) and qualitative (smoke flow visualization) results were 10 m/s. The corresponding chord-based Reynolds number was 76 K.

The object of this work was to document the effect of the plasma actuators in controlling the oscillatory lift and moment cycles as well as cycle hysteresis. For this, the plasma actuator was operated in both steady and unsteady modes over the full and partial oscillatory cycles.

A. Steady Actuation

The pressure coefficient distributions on the suction surface of the airfoil during the pitch-up motion of the oscillatory cycle are shown in Fig. 6. The percent uncertainty in all of the coefficient of pressure data is 1.7%. The left plot corresponds to the natural condition with the actuator off. In this case, the C_p values peak at $\alpha = 21$ deg, with a maximum $C_p \simeq -4$. As the pitch cycle continues, the peak $-C_p$ diminishes and a broad bulge in the C_p distribution appears. This bulge is a characteristic of the dynamic stall vortex. Subsequent angles in the pitching cycle show the movement of the bulge toward the trailing edge as the dynamic stall vortex convects downstream.

The pressure distributions as the airfoil pitches up with the steady actuator on are shown in the right plot of Fig. 6. In this case, the $-C_p$ peak is larger, approximately -5.75. In addition, the steady plasma actuator has suppressed the formation of the dynamic stall vortex. This is evident by the lack of the characteristic bulge in the C_p distributions at the higher angles of attack.

The coefficients of lift and moment for the oscillatory cycle were determined by integrating the pressure distribution around the airfoil for the different discrete angles. The total lift cycle and moment coefficient cycle are presented in Fig. 7. The percent uncertainty in all of the coefficient of lift results is 1.9%. The uncertainty in the pitch-moment results is 2.2%. The data presented in Fig. 7 corresponds to two cases: the actuator off (small, filled square symbols) and the steady actuator on over the entire cycle (open circle symbols).

The left plot in Fig. 7 shows the lift coefficient cycle for both the actuator-off and open-loop control, steady-actuator-on cases. The actuator-off case has the characteristic shape observed by others [31]. Up to approximately $\alpha = 22$ deg during the pitch-up portion of the cycle, a near linear increase in the lift exists with increasing angle of attack. Above this angle of attack, there is a sharp increase in the lift coefficient. This increase in lift is associated with the formation of the dynamic vortex. The vortex forms at the leading edge, is shed, and convects downstream over the surface of the airfoil. After the vortex leaves the trailing edge of the airfoil, the flow fully separates as indicated by the sharp drop in the lift past α_{max}.

With the actuator on, there is a slight lift improvement over most of the cycle. In particular, during the pitch-up motion of the cycle, there is a higher lift coefficient at all angles below $\alpha = 20$ deg. Because the plasma actuator has suppressed the dynamic stall vortex, the lift associated with the vortex is also suppressed. This is evident from the elimination of the sharp increase in lift previously seen at $\alpha = 22$ deg and the lobe in the lift cycle in the initial pitch-down portion. Past this

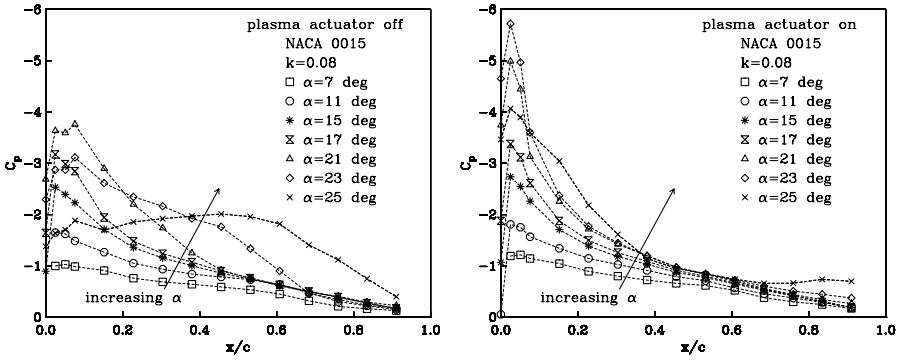

Fig. 6 Coefficient of pressures for the suction surface of the airfoil as it pitches up in the oscillatory cycle. Percent uncertainty in C_p is 1.7% and in α is 2%.

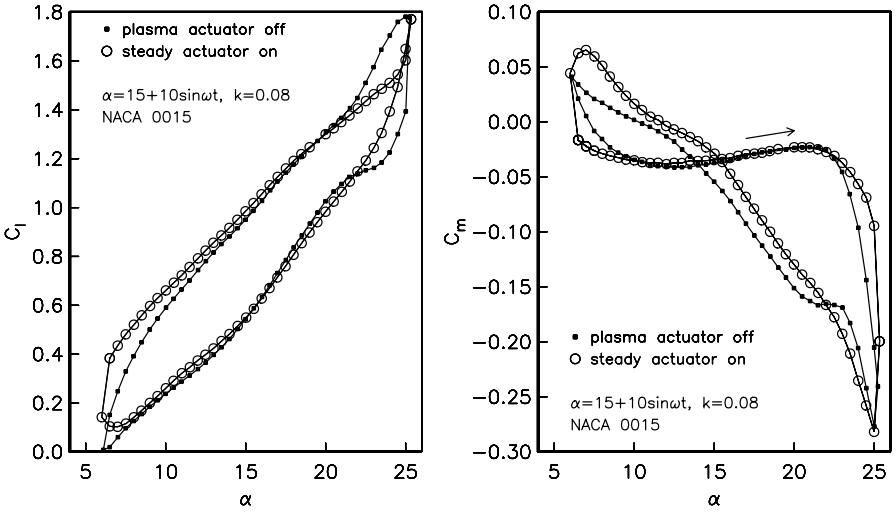

Fig. 7 Comparison of coefficient of lift vs angle of attack and the moment coefficient vs angle of attack for the case of steady actuation. Percent uncertainty in C_l is 1.9%, in C_m is 2.2%, and in α is 2%.

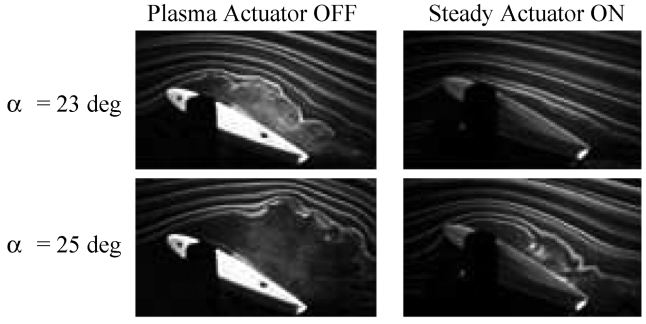

Fig. 8 Flow visualization records for the plasma actuator off and the steady plasma actuator on at $\alpha = 23$ deg during pitch up and $\alpha = 25$ deg at the peak angle of attack.

part of the cycle, however, during the remainder of the pitch-down motion, a lift improvement occurs with the plasma actuator on. The peak coefficient of lift is the same for both cases.

The right plot in Fig. 7 shows the moment coefficient cycle for both the actuator-off and open-loop control, steady-actuator-on steady cases. The stall in the moment curve indicates the formation of the dynamic stall vortex. The actuator has delayed slightly the moment stall, but has not reduced the large negative peak in the moment coefficient cycle.

Flow visualization records that are phased with the oscillatory motion are used to obtain a better understanding of the flow phenomena. Figure 8 shows that at $\alpha = 23$ deg with no actuation, the flow is visibly separated at the leading edge, and the dynamic stall vortex is visible at the midchord location of the airfoil. At $\alpha = 23$ deg, the steady plasma actuator maintains a completely attached flow at the leading edge, suppressing the formation of the dynamic stall vortex.

At the maximum angle of attack in the cycle, $\alpha = 25$ deg, the flow visualization with the plasma actuator off indicates that the flow is completely separated. The mixed smoke near the center of the airfoil's surface appears to show a coherent feature that, when compared with the C_p distributions, correspond to the dynamic vortex. With the open-loop control, steady plasma actuator on, only a small separation bubble exists near the leading edge of the airfoil.

B. Unsteady Plasma Actuation

The optimal unsteady forcing frequency for a static airfoil is when the Strouhal number, $St = fc/U_\infty$, is near unity. In this equation, f is the actuator forcing frequency, c is the separation length (which, in the case of the full leading-edge separation, is the airfoil chord length), and U_∞ is the freestream velocity. This optimal frequency is based on maintaining (including generation and convection) 2–3 vortical structures over the separated length at any given instant in time. If it were assumed for this experiment that the optimal forcing

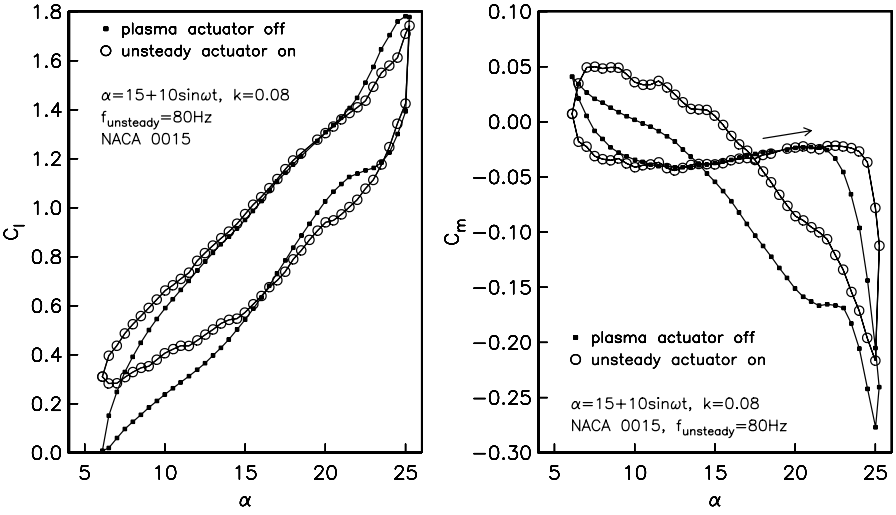

Fig. 9 Comparison of coefficient of lift vs angle of attack and moment coefficient vs angle of attack for the case of 80 Hz unsteady plasma actuation. Percent uncertainty in C_l is 1.9%, in C_m is 2.2%, and in α is 2%.

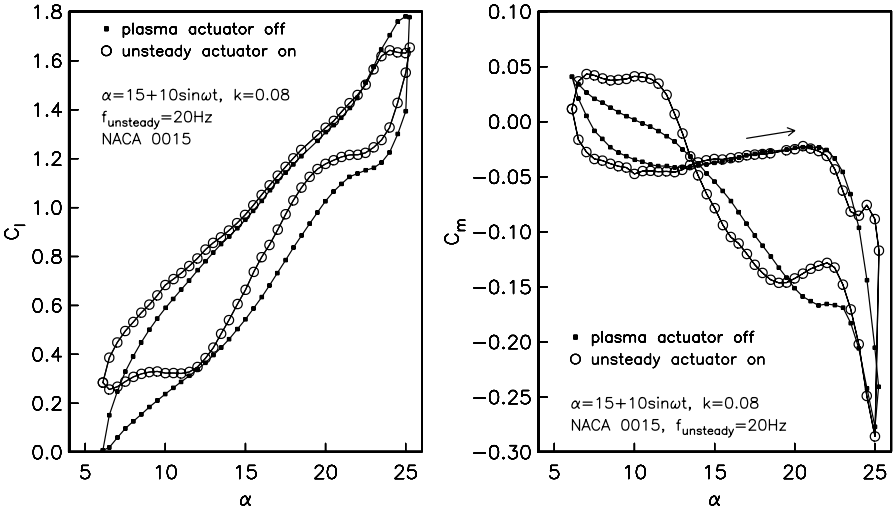

Fig. 10 Comparison of coefficient of lift vs angle of attack and moment coefficient vs angle of attack for the case of 20 Hz unsteady plasma actuation. Percent uncertainty in C_l is 1.9%, in C_m is 2.2%, and in α is 2%.

frequency was at $St = 1$, c was 12.7 cm (5 in.), and U_∞ was 10 m/s, then the corresponding optimal forcing frequency was $f = 80$ Hz. Because this empirical equation has been shown to be efficient for static airfoils and not dynamically oscillated airfoils, factors of this forcing frequency were also investigated. This paper documents the results for $f = 80$ and $f = 20$ Hz.

Figure 9 presents the lift and moment coefficient cycles for the unforced and 80 Hz unsteady-actuation cases. Recall that the same 5 kHz driving frequency was used to generate the plasma, but the amplitude was impulsively turned on and off at a frequency of 80 Hz (see Fig. 5 for waveform illustration). This unsteady forcing frequency was not phased with the 4 Hz physical oscillation frequency of the airfoil. A duty cycle for the unsteady forcing was 10%. This means that the actuator was activated only 10% of the time compared with steady operation, reducing the input power by 90%.

Comparing the lift coefficient cycle with the 80 Hz actuation (open circle symbols in Fig. 9) with that without actuation (small, filled square symbols in Fig. 9) and the steady actuation (open circle symbols in Fig. 7), considerable differences can be observed. In particular, the 80 Hz forcing increased the lift at the lower angles of attack in the pitch-down portion of the cycle. However, at the beginning of the pitch-down phase, the lift is lower compared with either the no-actuation or steady-actuation cases. In addition, the unsteady actuation at 80 Hz let the undesirable large C_l drop past $\alpha_{\max}$.

In contrast to the lift cycle, the moment coefficient cycle, shown in the right plot of Fig. 9, has some dramatic improvements with the 80 Hz actuation. The moment stall was delayed by more than 2 deg. The negative peak had been reduced by 18%. The negative aerodynamic damping had been reduced and the positive damping had increased.

To contrast the results of the 80 Hz unsteady actuator, the lift and moment coefficient cycles with a four times lower actuator frequency of 20 Hz were investigated. This unsteady frequency of 20 Hz was still five times the physical oscillatory frequency of the airfoil. Figure 10 shows some key differences between the unforced and 20 Hz unsteady actuator cases. There is a higher lift over the entire pitch-down portion of the cycle, which is most noticeable in the range from 25 deg $\geq \alpha \geq$ 13 deg. In addition, the airfoil maintains a higher lift at the bottom of the pitch-down phase that persists through the first half of the pitch-up phase. All of these are positive effects toward increasing the cycle-integrated lift. There is, however, a slight reduction in the peak lift at $\alpha_{\max}$ that was not evident in the steady or 80 Hz actuator cases. The moment coefficient cycle does not, however, display the improvements observed with the actuator operated at 80 Hz.

To obtain a better understanding of how the unsteady actuator may have affected the flow over the oscillatory airfoil, flow visualization

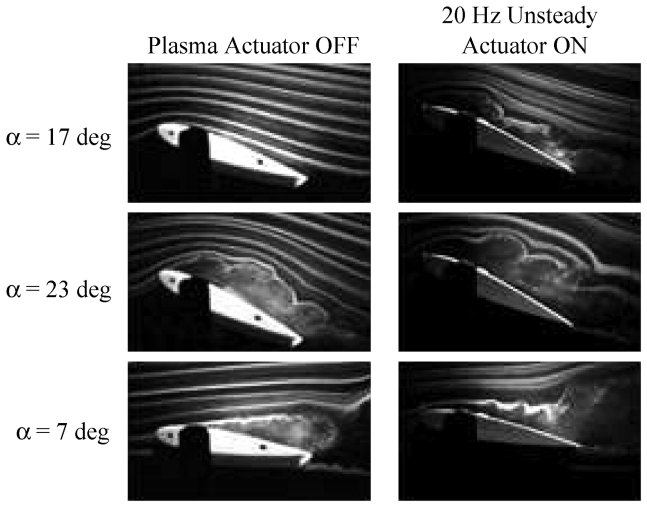

Fig. 11 Flow visualization records at $\alpha = 17$ deg and $\alpha = 23$ deg during pitch up and $\alpha = 7$ deg during pitch down.

was examined. Figure 11 shows three angles of attack in the cycle, 17 and 23 deg in the pitch-up phase of the cycle and at 7 deg in the pitch-down phase of the cycle with the actuators off (in the left column) and the 20 Hz unsteady actuator on (in the right column). All of the images for the unsteady actuated case show a train of periodic vortex-shaped structures on the upper surface of the airfoil. This regular pattern of vortices produced by the unsteady actuation is well defined and there appear to be three structures per chord length. Note that the optimal frequency scaling for the control of flow separation is based on having two spanwise vortices in the length of the separation bubble [25], which, in this case, is the wing chord. However, the penalty in being off of the optimal frequency was found to be more severe at frequencies lower than the optimum than those higher than the optimum [25]. Thus, the 20 Hz is still effective. At $\alpha = 7$ deg, the 20 Hz unsteady actuation results in a faster reattachment, as indicated visually in Fig. 11 and as illustrated in Fig. 10 by the added lift in that portion of the cycle.

C. Closed-Loop Control Plasma Actuation

By observing the effects that steady and unsteady plasma actuators had on controlling the dynamic stall vortex and altering the oscillatory lift cycle, a closed-loop control actuator was designed. It was designed to operate only during *portions* of the airfoil's

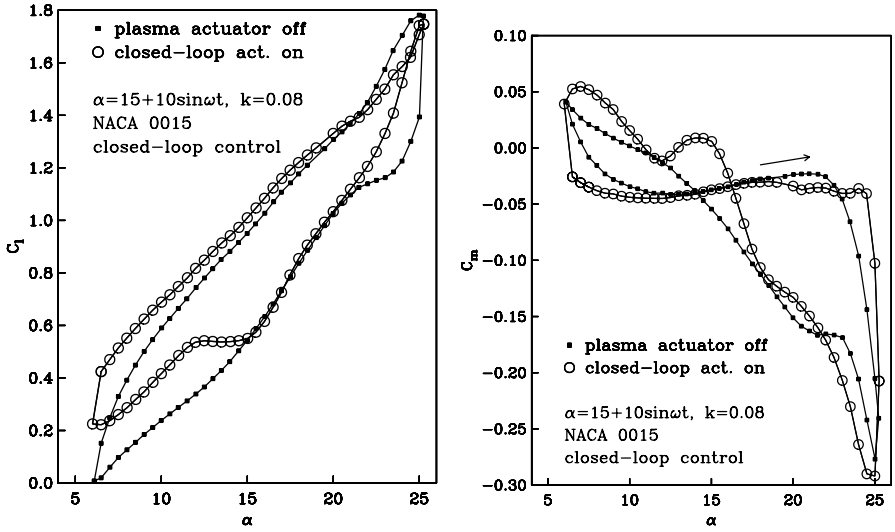

Fig. 12 Comparison of coefficient of lift vs angle of attack and moment coefficient vs angle of attack for the case of closed-loop control plasma actuation. Percent uncertainty in C_l is 1.9%, in C_m is 2.2%, and in α is 2%.

oscillatory cycle. These portions were defined as a range of angles of attack where the actuation was intended to augment the lift.

To accomplish this, a circuit was built that used the airfoil angle-of-attack information from the motor encoder as an input and selectively turned the actuator on or off during predetermined portions of the oscillatory cycle. During the on time, the actuator functioned in either the steady or unsteady operation. The results presented in this paper correspond only to the steady actuator operation.

The ranges of angles of attack in the airfoil's oscillatory cycle when the actuator was set to be on were: 1) 15 deg $\leq \alpha \leq$ 20 deg during the pitch-up phase; 2) 24 deg $\leq \alpha \geq$ 23 deg during the pitch-up phase, through the peak angle of attack; and 3) 20 deg $\geq \alpha \geq$ 8 deg during the pitch-down phase.

The rational for operating the actuator between 15 deg $\leq \alpha \leq$ 20 deg was to keep the flow attached during the high angles of attack of the pitch-up portion of the cycle. It was subsequently turned off from 21 deg $\leq \alpha \leq$ 23 deg during pitch up to allow the dynamic vortex to form. Previous cases showed that if the actuator suppressed the formation of the vortex, the increase in lift associated with the vortex would also be suppressed.

The actuator was turned back on just before the peak angle was reached, between $\alpha = 24$ deg in the pitch up and $\alpha = 23$ deg in the pitch down. This was intended to reduce dynamic stall and thereby eliminate the sharp drop in lift that typically occurs as the airfoil passes the maximum angle of attack.

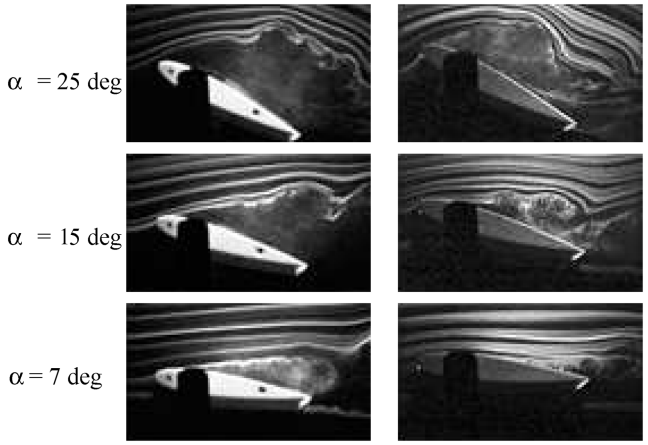

Fig. 13 Flow visualization records for the plasma actuators off (left column) and closed-loop control plasma actuation (right column).

In the pitch-down portion of the cycle, the actuator is turned off at $\alpha = 22$ deg, but turned on again at $\alpha = 20$ deg, where it remains on until the angle of attack is near the minimum. The reason for this was to initiate a disturbance at the leading edge to bring high momentum flow near the surface and reattach the flow as soon as possible in the pitch down, which could have potentially reduced the lift-cycle hysteresis.

Figure 12 shows a comparison of the lift and moment coefficient cycles for the actuator-off and closed-loop control actuator cases. With the closed-loop control actuation, there was an increase in the lift over the complete cycle. In particular, a significant improvement in the lift during the pitch-down portion of the cycle, especially at the lower angles of attack, was observed. Following α_{max}, the sharp stall that gave the lift cycle the lobed shape with the actuators-off case was replaced with a more desirable smooth lift decrease with less hysteresis. The high peak in the coefficient of lift was also maintained.

With regard to the moment cycle, the moment stall has been delayed three deg, which was approximately a degree better than the 80 Hz unsteady actuation. However, the negative peak in the moment cycle was slightly greater in magnitude than in the no-control case, which was a negative effect.

The flow visualization results presented in Fig. 13 illustrate some of the differences in the flowfield produced with the actuators off (left column) and closed-loop control actuators (right column). It represents three angles of attack in the cycle: $\alpha = 25$ deg, $\alpha = 15$ deg, and $\alpha = 7$ deg. These angles, the peak angle of attack and two during the pitch-down portion of the cycle, were highlighted because they displayed some of the most dramatic differences between the cases.

Figure 13 shows that both approaches are able to reattach the flow at the leading edge by $\alpha = 7$ deg. However, the closed-loop control is more effective at reattaching the flow, with a visible reattachment occurring at $\alpha = 15$ deg, the earliest of any of the four cases investigated. Achieving reattachment as soon as possible in the pitch-down portion of the cycle is important in reducing the lift hysteresis.

IV. Discussion

A comparison of the amount of lift improvement that was obtained for each controlled case is presented in Table 2. The improvement was determined by integrating under the total lift-cycle curve for each case and dividing by the integrated lift of the no-actuation case. The results show that the closed-loop control provided the largest lift improvement of 12.6% compared with no control. The second best at a 10.1% improvement was the 20 Hz unsteady case. The steady case

Table 2 Comparison of lift improvement

Scheme	% Lift improvement
80 Hz unsteady	4.7
Steady	5.4
20 Hz unsteady	10.1
Closed-loop control	12.6

was the third best with a 5.4% improvement, followed by the unsteady 80 Hz case, which showed a 4.7% increase in the lift. Any of these is a significant improvement over the no-actuation case. Note that from the perspective of the lift-moment cycle, the 80 Hz was the best, followed by the closed-loop control case.

From a systems standpoint, the closed-loop control and unsteady actuation schemes are particularly attractive because the actuator is not operating over the entire cycle for the closed-loop control actuation and is operating at only a 10% duty for the unsteady actuation. Therefore, the total power is reduced compared with the steady-actuation case.

The flow visualization results for the four cases of no actuation, steady actuation, 20 Hz unsteady actuation, and closed-loop control actuation are directly compared in Fig. 14. From these records, it is clear that any of the actuator cases maintain an attached flow in the pitch-up portion of the cycle at higher angles compared with the no-actuator case. The best of these from this perspective was the steady actuator that was on throughout the cycle. As the lift cycles revealed, this was not the best from the point of view of reaching a peak lift. In contrast to the steady actuator, the flow visualization for the 20 Hz and closed-loop actuation cases show the formation of the dynamic stall vortex just before the peak angle of attack, which was found to enhance the peak lift.

The 20 Hz and closed-loop actuator cases were the most effective in reattaching the flow in the pitch-down portion of the cycle. This is evident in the bottom three rows of the images in Fig. 14. Of these two cases, the best from this aspect was the closed-loop control case. This accounts for the larger lift produced in this part of the cycle. Overall, the flow visualization records are consistent with the cycle lift measurements.

A. Strategy for Closed-Loop Control

The closed-loop control, which was based on the angle of attack of the airfoil during the oscillation cycle, provided the best lift-cycle improvement. Although this type of control scheme is possible in

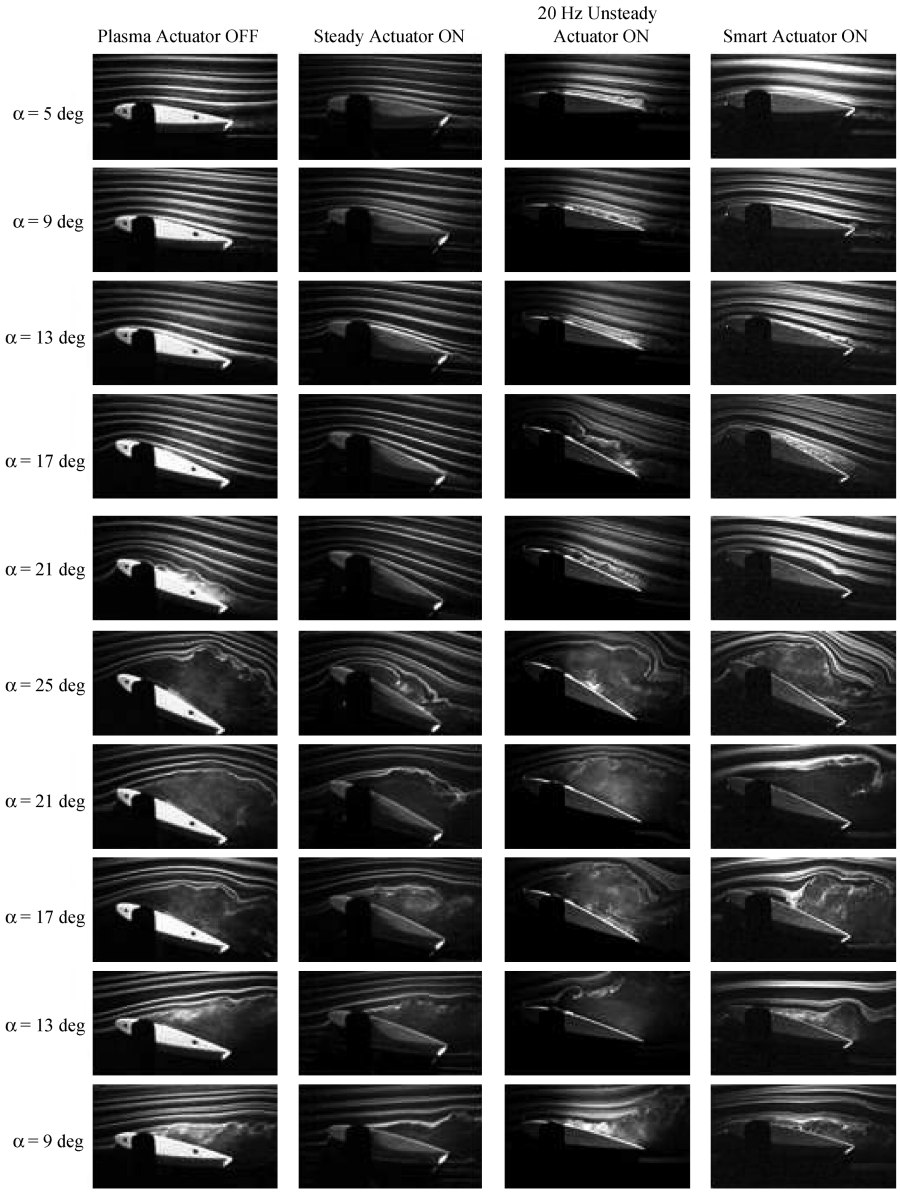

Fig. 14 Flow visualization records for no actuation, steady plasma actuation, unsteady plasma actuation, and closed-loop control actuation.

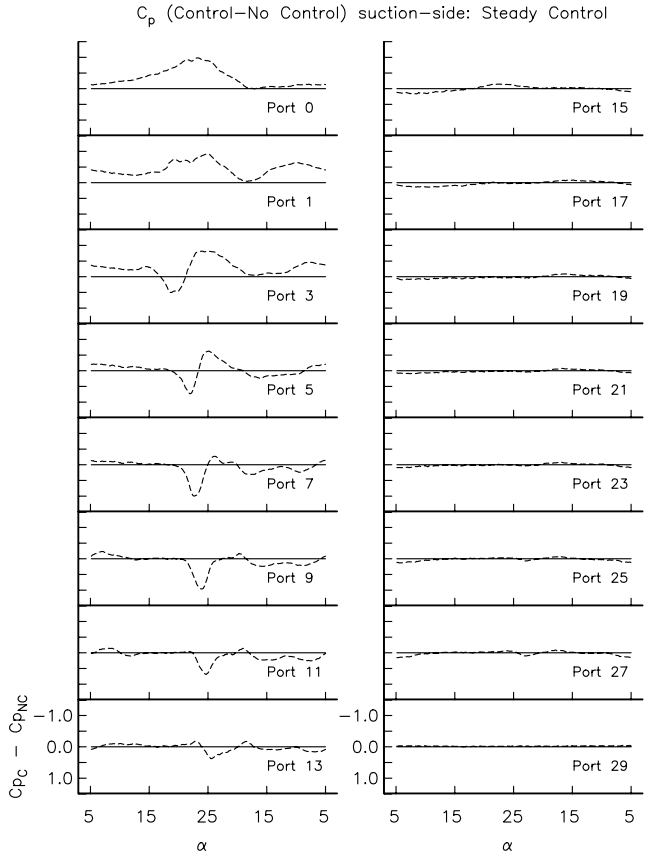

Fig. 15 Difference between the coefficient of pressure for the no-actuation and steady-actuation cases. Port 0 is at the leading edge. Percent uncertainty in C_p is 1.6% and in α is 2%.

real applications like helicopter rotors, it is more likely that in situ flow measurements will be required to provide information on the state of the flow to determine optimum actuator operation. Therefore, this section seeks to capture features of the airfoil surface pressure distribution that can be used for feedback control.

The basis of comparison is ensemble-averaged C_p distributions on the suction side of the oscillating airfoil. A local indication of the effectiveness of the control approach could be the difference between C_p values at a port location without and with actuation, as illustrated in Fig. 15. Port 0 is at the leading edge. The increasing port numbers correspond to increasing x/c locations. The exact locations of the port numbers are given in Table 1. Figure 15 shows the difference between the ensemble-averaged values over one cycle at the different port positions. The difference is taken as $C_{p_C} - C_{p_{NC}}$, where subscript C refers to the case with control and NC refers to the case with no control. If the difference is negative, indicated above the horizontal line at $C_p = 0$, it represents an improvement over the no-control case.

It is evident from Fig. 15 that there is little difference between the C_p values with the actuator off and on at locations beyond port 15, which corresponds to $x/c > 0.456$. This means that the effect of the plasma actuator is primarily upstream of this location. It indicates that from a control approach that is based on pressure measurements on the airfoil's surface, the sensor's location needs to be upstream of the 45% chord position.

The magnitude of the differences between the C_p values depends on the x/c location on the airfoil and angle of attack in the oscillating cycle. For example, at the leading edge (port 0), the differences in C_p are most apparent near the maximum angle of attack. As the measurement position moves aft (or port number increases), the portion of the oscillatory cycle where the difference between control and no control is most evident shifts toward pitch down.

With steady actuation, previous results have indicated a negative effect on lift by completely suppressing the formation of the dynamic vortex. The signature of this is the dip in the C_p difference between ports 3–13 at the high angles of attack in the pitch-up portion of the cycle. This is precisely the portion of the cycle where the dynamic vortex first forms.

A comparison between the two unsteady-actuation cases and the no-actuation case are made in Fig. 16. Recall that based on integrated lift, the 20 Hz was better than the 80 Hz unsteady case. When the ensemble-averaged C_p distributions are compared, this result becomes clear. Near the leading edge (ports 0–3), the 80 Hz unsteady control results in the highest $-C_p$ values. This indicates that the 80 Hz unsteady actuation was better in keeping the leading-edge flow attached than the 20 Hz unsteady actuation. However, further back from the leading edge (ports 7–13), the 20 Hz unsteady control produces larger $-C_p$ values. These improvements also appear primarily in the pitch-down part of the cycle, indicating that the 20 Hz unsteady actuation was better in reattaching the flow at that location.

These results indicate that there may not be a single optimal unsteady actuator frequency to improve the lift cycle and cycle hysteresis. And that, in fact, another scheme might be to change the unsteady frequency during the oscillating cycle. For example, the 80 Hz frequency could be used in the pitch-up portion and the 20 Hz frequency used during the pitch-down portion to use the advantages of each scheme.

Figure 17 shows the differences between the C_p distributions of the steady, 20 Hz unsteady, and closed-loop control actuations. Near the leading edge (ports 0 and 1), the steady and closed-loop control actuation produce a comparable improvement during pitch up. However, also based on these port locations, the closed-loop control actuation produces a larger $-C_p$ at the lower angles of attack during pitch down. This would signify that the closed-loop control actuation is reattaching the flow sooner.

The 20 Hz unsteady actuation provides a better improvement downstream of the airfoil's leading edge (ports 7 and 9) at the high angles of attack during pitch down. However, the magnitude of those improvements are smaller than those obtained elsewhere with the closed-loop control actuation, so that averaging over the whole cycle, the closed-loop control actuation produces the largest lift improvement.

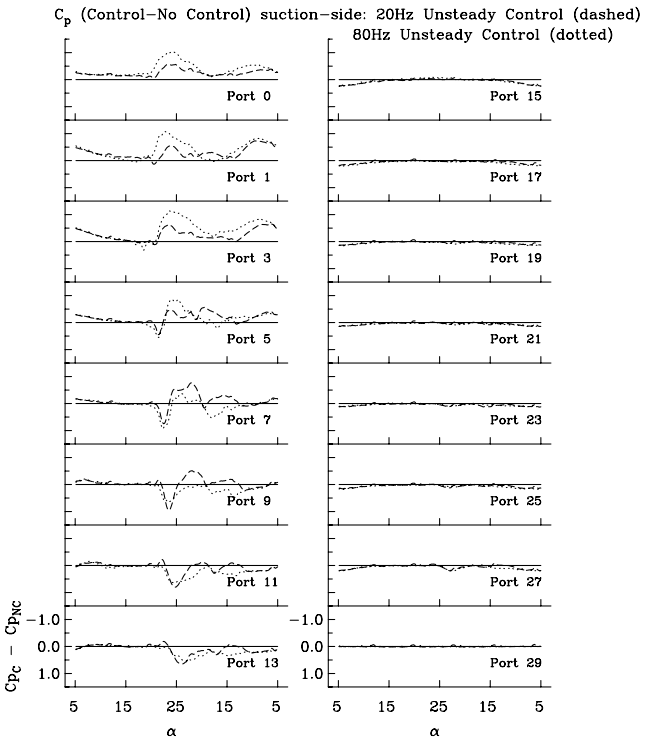

Fig. 16 Difference between the coefficient of pressure for the no-actuation and unsteady-actuation cases. Percent uncertainty in C_p is 1.6% and in α is 2%.

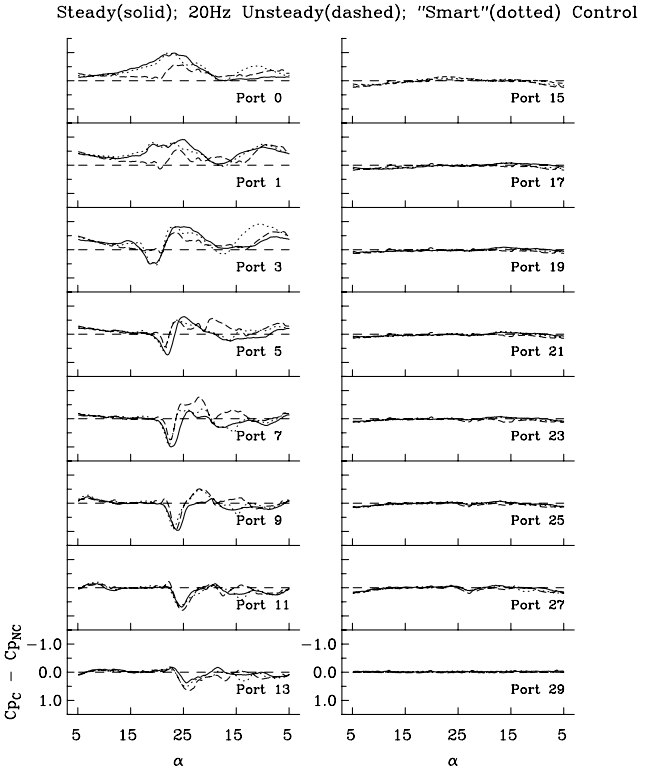

Fig. 17 Difference between the coefficient of pressure for the no-actuation, 20 Hz unsteady actuation, and smart actuation cases. Percent uncertainty in C_p is 1.6% and in α is 2%.

V. Summary

The use of plasma actuators for leading-edge separation and dynamic stall vortex control on a periodically oscillating NACA 0015 airfoil was investigated. The actuator's effectiveness was based on a combination of quantitative pressure measurements on the surface of the airfoil and qualitative smoke flow visualization records.

The results for a sinusoidally oscillated airfoil with a mean angle of attack of 15 deg and an amplitude of plus or minus 10 deg with a reduced frequency of 0.08 were presented. Three cases with the plasma actuator were documented here: 1) open-loop control with a steady actuator operation, 2) open-loop control with unsteady actuator operation, and 3) closed-loop control with steady actuator operation over parts of the airfoil pitching cycle.

All of the actuator cases were found to improve the lift cycle. The steady plasma actuation increased the lift over most of the cycle, except at the peak angle of attack where it was found to suppress the dynamic stall vortex. The principle advantage of this was that the steady actuator eliminated the sharp drop in the lift coefficient at the start of the pitch down that is associated with the dynamic stall.

The unsteady plasma actuation produced significant improvements in the lift coefficient during the pitch-down phase of the cycle, especially near the minimum angle of attack. For lift-cycle improvement, the best actuator frequency appeared to be at a dimensionless frequency of 0.25. For delaying moment stall and reducing the negative peak in the moment curve, the best actuator frequency was at a dimensionless frequency of unity. A closed-loop control actuator approach produced the greatest improvement in the lift cycle with the highest integrated lift and elimination of the sharp stall past the maximum angle of attack.

Acknowledgment

This work was supported by a grant from the Defense Advanced Research Projects Agency/Army Research Office, number DAAD19-00-1-0447. The U.S. government is authorized to reproduce and distribute reprints for government purposes, not withstanding any copyright notation therein.

References

[1] Lorber, P., McCormmick, D., Anderson, T., Pollack, M., Corke, T., and Breuer, K., "Rotorcraft Retreating Blade Stall Control," AIAA Paper 2000-2475, 2000.

[2] Aiken, E., Ormiston, R., and Young, L., "Future Directions in Rotorcraft Technology at Ames Research Center," *Proceedings of the American Helicopter Society's 56th Annual Forum* [CD ROM], American Helicopter Society, Alexandria, VA, 2000.

[3] Carr, L., and Chandrasekhara, M., "Compressibility Effects on Dynamic Stall," *Progress in Aerospace Sciences*, Vol. 32, No. 6, 1996, pp. 523–573.

[4] Lorber, P., and Carrta, F., "Airfoil Dynamic Stall at Constant Pitch Rate and High Reynolds Number," *Journal of Aircraft*, Vol. 25, June 1988, pp. 548–556.

[5] Lorber, P., "Compressibility Effects on the Dynamic Stall of a Three-Dimensional Wing," AIAA Paper 1992-0191, Jan. 1992.

[6] Visbal, M., "Effect of Compressibility on Dynamic Stall of a Pitching Airfoil," AIAA Paper 1988-0132, Jan. 1988.

[7] Grohsmyer, S., Ekaterinaris, J., and Platzer, M., "Numerical Investigation of the Effect of Leading Edge Geometry on Dynamic Stall of Airfoils," AIAA Paper 1989-0024, Jan. 1989.

[8] Patterson, M., and Lorber, P., "Computational and Experimental Studies of Compressible Dynamic Stall," *Journal of Fluids and Structures*, Vol. 4, 1990, pp. 259–285.

[9] Friedman, P., and Millot, T., "Vibration Reduction in Rotorcraft Using Active Control: A Comparison of Various Approaches," *American Helicopter Society Aeromechanics Specialists Conference* [CD ROM], American Helicopter Society, Alexandria, VA, 1994.

[10] Lorber, P., Stauter, R., Hass, R., Anderson, T., Torok, M., and Kohlhepp, F., "Techniques for Comprehensive Measurement of Model Helicopter Rotor Aerodynamics," *50th Annual Forum of the American Helicopter Society* [CD ROM], American Helicopter Society, Alexandria, VA, 1994.

[11] Bousman, W., "A Quantitative Examination of Dynamic Stall from Flight Test Data," *Journal of the American Helicopter Society*, Vol. 43, Oct. 1998, pp. 279–295.

[12] Corke, T., *Design of Aircraft*, Prentice–Hall, New York, 2002.

[13] Narramore, J., McCroskey, W., and Noonan, K., "Design and Evaluation of Multi-Element Airfoils for Rotorcraft," *Proceedings of the American Helicopter Society's 55th Annual Forum* [CD ROM], American Helicopter Society, Alexandria, VA, 1999.

[14] Yu, Y., McAlister, K., Tung, C., and Wang, C., "Dynamic Stall Control for Advanced Rotorcraft Application," *AIAA Journal*, Vol. 33, No. 2, 1995.

[15] Karim, M., and Achyara, M., "Control of the Dynamic Stall Vortex Over a Pitching Airfoil by Leading Edge Suction," AIAA Paper 1993-3267, July 1993.

[16] Post, M. L., "Plasma Actuators for Separation Control on Stationary and Oscillating Airfoils," Ph.D. Dissertation, Univ. of Notre Dame, Notre Dame, IN, Apr. 2004.

[17] Enloe, L., McLaughlin, T., VanDyken, R., Kachner, K., Jumper, E., Corke, T., Post, M., and Haddad, O., "Mechanisms and Response of a Single Dielectric Barrier Plasma Actuator: Geometric Effects," *AIAA Journal*, Vol. 42, No. 3, 2004, pp. 595–604.

[18] Seifert, A., Bachar, T., Moss, D., Shepshelovish, M., and Wygnanski, I., "Oscillatory Blowing: A Tool to Delay Boundary-Layer Separation," *AIAA Journal*, Vol. 11, No. 31, 1993, pp. 2052–2060.

[19] Seifert, A., Darabi, A., and Wygnanski, I., "Delay of Airfoil Stall by Periodic Excitation," *Journal of Aircraft*, Vol. 33, No. 4, 1996, pp. 691–698.

[20] Seifert, A., and Pack, L., "Oscillatory Excitation of Unsteady Compressible Flows Over Airfoils at Flight Reynolds Numbers," AIAA Paper 99-0925, 1999.

[21] Greenblatt, D., and Wygnanski, I., "The Control of Separation by Period Excitation," *Progress in Aerospace Sciences*, Vol. 36, No. 7, 2000, pp. 487–545.

[22] Corke, T., Jumper, E., Post, M. L., Orlov, D., and McLaughlin, T., "Application of Weakly-Ionized Plasmas as Wing Flow-Control Devices," AIAA Paper 2002-0350, Jan. 2002.

[23] Huang, J., Corke, T., and Thomas, F., "Plasma Actuators for Separation Control of Low Pressure Turbine Blades," AIAA Paper 2003-1027, Jan. 2003.

[24] Post, M. L., and Corke, T., "Separation Control on High Angle of Attack Airfoil Using Plasma Actuators," *AIAA Journal*, Vol. 42, No. 11, 2004, pp. 2177–2184.

[25] Corke, T., He, C., and Patel, M., "Plasma Flaps and Slats: An Application of Weakly-Ionized Plasma Actuators," AIAA Paper 2004-2127, 2004.

[26] Wilkinson, S. P., "Investigation of an Oscillating Surface Plasma for Turbulent Drag Reduction," AIAA Paper 2003-1023, 2003.
[27] Thomas, F. O., Koslov, A., and Corke, T. C., "Plasma Actuators for Landing Gear Noise Reduction," AIAA Paper 2005-3010, 2005.
[28] Hultgren, L. S., and Ashpis, D. E., "Demonstration of Separation Delay with Glow Discharge Plasma Actuators," AIAA Paper 2003-1025, 2003.
[29] Mueller, T., "On the Historical Development of Apparatus and Techniques for Smoke Visualization of Subsonic and Supersonic Flows," AIAA Paper 80-0420-CP, 1980.
[30] Enloe, L., McLaughlin, T., VanDyken, R., Kachner, K., Jumper, E., and Corke, T., "Mechanisms and Response of a Single Dielectric Barrier Plasma Actuator: Plasma Morphology," *AIAA Journal*, Vol. 42, No. 3, 2004, pp. 589–594.
[31] Leishman, J. G., *Principles of Helicopter Aerodynamics*, Cambridge Univ. Press, New York, 2000.

N. Chokani
Associate Editor